LA-UR 04-3201,
to be published in J. Acoust. Soc. Am.

A resonant, self-pumped, circulating thermoacoustic heat exchanger

G. W. Swift and S. Backhaus

Condensed Matter and Thermal Physics Group,

Los Alamos National Laboratory,

Los Alamos, New Mexico 87545 *

(Dated: August 12, 2004)

Abstract

An asymmetrical constriction in a pipe functions as an imperfect gas diode for acoustic oscillations in the pipe. One or more gas diodes in a loop of pipe create substantial mean flow, approximately proportional to the amplitude of the oscillations. Measurements of wave shape, time-averaged pressure distribution, mass flow, and acoustic power dissipation are presented for a two-diode loop. Analysis of the phenomena is complicated because both the mean flow and the acoustic flow are turbulent and each affects the other significantly. The quasi-steady approximation yields results in rough agreement with the measurements. Acoustically driven heat-transfer loops based on these phenomena may provide useful heat transfer external to thermoacoustic and Stirling engines and refrigerators.

PACS numbers: 43.35.Ud, 43.25.Nm, 43.25.Qp

I. INTRODUCTION

Stirling's hot-air engine[1,2] of the early 19th century was one of the first heat engines to use oscillating thermodynamics of a gas in a sealed system. Since then, a variety of related engines and refrigerators has been developed, including Stirling refrigerators,[1,3] Ericsson engines,[4] orifice pulse-tube refrigerators,[5] standing-wave thermoacoustic engines and refrigerators,[6] free-piston Stirling engines and refrigerators,[7] and thermoacoustic-Stirling hybrid engines and refrigerators (also known as traveling-wave systems).[8–11] Combinations thereof, such as the Vuilleumier refrigerator[12] and the thermoacoustically driven orifice pulse-tube refrigerator,[13] have provided heat-driven refrigeration. Today, the efficient, mature members of this family of engines and refrigerators are in use in several niche markets, ranging from small cryocoolers with cooling powers below 10 W to large engines (e.g., for submarine propulsion) with powers near 100 kW.

Much of the recent evolution of this family of oscillating-gas thermodynamic technologies has been driven by the search for simplicity, reliability, and low fabrication costs through the elimination of moving parts, especially elimination of moving parts at temperatures other than ambient temperature, without seriously compromising efficiency. For example, the orifice pulse-tube refrigerator lacks the cold piston of previous cryogenic Stirling refrigerators; the free-piston Stirling engine lacks the crankshafts and connecting rods present in previous Stirling engines; and the thermoacoustic-Stirling hybrid engine eliminates pistons previously needed.

Heat exchangers may offer a second opportunity for dramatic improvement in simplicity, reliability, and low fabrication cost, particularly in engines and refrigerators of high power. All engines and refrigerators must reject waste heat to ambient temperature, and the ambient heat sink is often available as a flowing air stream or water stream. Engines must also accept heat from a heat source at a higher temperature, e.g., a stream of combustion products from a burner. Refrigerators must withdraw heat from a load at lower temperature, which is sometimes in the form of a flowing stream; examples include a stream of indoor air to be cooled and dehumidified and a stream of oxygen to be cooled and cryogenically liquefied. Hence, the typical heat exchanger in these engines and refrigerators must transfer heat between a steadily flowing "process fluid" stream such as these and the oscillating thermodynamic "working gas" (often pressurized helium).

In large, high-power engines and refrigerators, the thermal conductivity of solids is insufficient to carry the required heats without significant temperature differences, so geometrically complicated heat exchangers must usually be used to interweave the process fluid and the working gas, bringing them into intimate thermal contact. A shell-and-tube heat exchanger[14] is typical. In the orientation of Fig. 1(a), the working gas oscillates vertically through the insides of the many tubes, while the process fluid flows horizontally around and between the outsides of the tubes. Features specific to oscillating-gas engines and refrigerators impose unfortunate constraints on such heat exchangers as they are scaled up to higher power. Higher power demands more heat-transfer surface area, lest the efficiency suffer. However, tube lengths cannot be increased, because having such tube lengths greater than the oscillatory stroke of the working gas does not effectively transfer more heat. Hence, the obvious approach to scaleup is to increase the number of tubes in proportion to the power, keeping the length and diameter of each tube constant. Such heat exchangers can have hundreds or thousands of tubes, causing expense (because many parts must be handled, assembled, and joined) and unreliability (because many joints must be leak tight). Thermally induced stress poses an additional challenge to reliability when such a geometrically complex heat exchanger is at an extreme temperature, i.e., a red-hot temperature for an engine or a cryogenic temperature for a refrigerator.

Another shortcoming of the heat exchangers of oscillating-gas engines and refrigerators is that they often must be located close to one another, simply because each heat exchanger must be adjacent to one end or the other of the nearest stack, regenerator, pulse tube, or thermal buffer tube, and these components themselves are typically short. The practical importance of this shortcoming is easily appreciated by considering the food refrigerator in the typical American kitchen. Its "vapor compression" cooling technology allows complete flexibility in the geometrical separation of the cold heat exchanger, where heat is absorbed from the inside of the cold box, and the ambient heat exchanger, where waste heat is rejected to the air in the kitchen, typically behind or under the refrigerator cabinet. With vapor-compression technology, not only can these heat exchangers be located freely, but their shapes can be chosen as needed for their circumstances, e.g., to accommodate fan-driven or natural convection, and to fit in and around the desired shape of the cold box or cabinet. In contrast, when one tries to adapt an oscillating-gas refrigerator to this application, the

cold heat exchanger and ambient heat exchanger must be very close together, separated only by the regenerator or stack, whose length is typically only several centimeters. Hence, intermediate heat transfer equipment, such as heat pipes or pumped-fluid heat-transfer loops, must typically be used. These add complexity and expense.

To explore a new way to circumvent these shortcomings, we have begun to investigate the alternative heat-exchanger scheme illustrated in Fig. 1(b). This resonant, self-pumped, circulating thermoacoustic heat exchanger is a single pipe (or a few in parallel), which could be bent or coiled compactly, with a length equal to one wavelength of sound in the working gas in the pipe at the frequency of the engine's or refrigerator's oscillation. Both ends of the pipe are attached as "branches" to the "trunk" where a traditional heat exchanger would be expected. Oscillations of the gas in the pipe are caused by those in the trunk. Two gas diodes are in the pipe, each located a quarter wavelength from one end of the pipe. These create nonzero mean flow, so the motion of the working gas in the circulating heat exchanger is a superposition of oscillating flow and steady flow. Most of the extensive outside surface area of the pipe is available for thermal contact with the process fluid, which can flow either parallel or perpendicular to the pipe. The mean flow in the loop carries heat between this surface area and the mixing chamber in the trunk.

The gas diodes are the key to the heat-transfer circulation in Fig. 1(b). These are nonlinear flow elements having different flow resistances for flow in different directions. Gas diodes are typically much less perfect than electronic diodes, often with a ratio of backward and forward flow impedances less than a factor of ten. Gas diodes include the vortex diodes described by Mitchell,[15] the valvular conduit described by Tesla,[16] and the conical and tapered structures called jet pumps in some recent publications.[10,17]

The fact that the length of the pipe in Fig. 1(b) is one wavelength of sound leads to beneficial features, illustrated in Fig. 1(c). The gas diodes are located where the oscillating volume velocity[18] is a maximum, so they can create a large time-averaged pressure difference and a large mean flow, as explained more fully below. Meanwhile, the ends of the pipe are locations of minimal oscillating volume velocity, so that connecting the pipe to the trunk perturbs the oscillations in the trunk minimally. Figure 1(c) illustrates such minimal perturbation with the pipe ends presenting a real impedance to the trunk, but a slightly shorter pipe would add a positive imaginary part to that impedance, which could be useful

for canceling unwanted compliance in the trunk. Estimates indicate that the mean flow can be many times larger than the oscillating flow amplitude where the pipe joins the trunk; Fig. 1(c) illustrates it as 2.4 times larger.

A non-resonant but otherwise similar concept was described by Mitchell[15] for a particular case: the heat exchanger at the ambient end of the pulse tube of an orifice pulse-tube refrigerator. Mitchell replaced this particular heat exchanger and the orifice by a heat-transfer loop containing one or more gas diodes to convert some of the oscillatory power in the wave into mean flow of the working gas around the loop. The dissipation in the gas diode(s) and other acoustic dissipation in the loop serve the dissipative function of the original orifice, and the surface area along the entire path length of the loop serves the function of the original heat exchanger.

We undertook the work described here to investigate the main issues that are involved with using the resonant self-pumped loop for heat transfer. The insulated, electrically heated or water-cooled resonant loop described below was attached at both ends to a mixing chamber, where the sound wave was generated by a motor-driven piston and where heat from the electrically heated loop was rejected to water-cooled heat exchangers. Thermocouples monitored the temperature rise as the gas circulated through the insulated, heated loop; pressure transducers detected the oscillatory pressure associated with the wave and the time-averaged pressures associated with the mean flow. Most features of the experimental results are explained qualitatively by treating the oscillatory and mean flows as independently superimposed except at the gas diodes. The use of the quasi-steady approximation to analyze interactions of the oscillatory and mean flows throughout the loop, occurring through the Doppler effect and the nonlinearity of turbulent flow resistance, provides a better, reasonably quantitative interpretation of the measurements. An appendix summarizes the most tedious aspects of the application of the quasi-steady approximation to this situation.

II. APPARATUS AND PRELIMINARY MEASUREMENTS

From among the low-cost gases, we chose argon at a mean pressure $p_m = 2.4$ MPa for this investigation, because its high density gives it a low sound speed and small viscous and thermal penetration depths, which helped to keep the size of the apparatus and the thermal

and acoustic powers small enough for easy experimentation. We chose $\sim$ 50 Hz for the operating frequency and $\sim$ 2 cm for the inside diameter of the pipe, for compatibility with a linear motor and piston (described below) that were available in our lab.

The apparatus is illustrated in Fig. 2. The one-wavelength loop shown in Fig. 2(a) had a total length of 6.33 m and was made mostly of seamless stainless-steel pipe with an inside diameter $D_{\rm pipe} = 2.21$ cm. Long-radius elbows and fittings[19] smoothly matched this pipe's inside diameter. A valve at the velocity node halfway around the loop, at the top of Fig. 2(a), could be used to stop and start the mean flow while leaving the acoustics mostly undisturbed. Two geometrically identical sets of piping—one with thermocouples, heaters, and thermal insulation, the other cooled by flowing water—could be easily interchanged as desired for different types of measurements. For example, equilibration of the temperature profile around the loop required hours with the insulated pipes, but steady state could be reached in a few minutes with the water-jacketed pipes.

Gas diodes were located 1/4 and 3/4 of the way around the loop. Each was a machined brass cylinder with fittings brazed onto the ends, as shown in Fig. 2(b). The inside surface was a smooth cone 13.3 cm long, tapering from the 2.21-cm diameter of the loop piping at its large end to $D_{\rm gd} = 1.4$ cm diameter at its small end, so the angle between the cone wall and the centerline was 1.75°. The inner edge at the small end was rounded with a radius of 2.3 mm. These dimensions were chosen to minimize acoustic power dissipation and to minimize the flow resistance into the small end while simultaneously generating a large time-averaged pressure difference, according to the analysis presented in Sec. IIIA.

Eight piezoresistive pressure transducers[20] were arrayed along the loop as shown in Fig. 2(a), and two more were located in the drive assembly as shown in Fig. 2(c). A lock-in amplifier[21] was used to measure their oscillating voltage amplitudes and phases to obtain the complex pressure amplitude p_1 at each location, and a 5-digit voltmeter was used to measure their average voltages for calibration checks and to obtain the second-order, time-averaged pressures $p_{2,0}$ associated in part with the mean flow around the loop.[22] The reference side of the pressure transducer near the piston in Fig. 2(c) was always at atmospheric pressure, while the reference sides of the other nine transducers were held at 2.4 MPa so that the temperature dependence of the transducers' gains did not interfere with the measurements of $p_{2,0}$—otherwise, a small drift in temperature would have caused a large

drift in average voltage, masking the small voltage changes due to time-averaged pressure. The four transducers closest to the two gas diodes were connected to the loop through thin-walled stainless-steel capillaries 4 cm long and 0.6 mm i.d. so that their temperatures were minimally affected by the wave in the pipe; this feature is discussed in more detail in Sec. IIIB. Simple modeling of the acoustics of these capillaries and the volumes associated with the transducers indicated that the amplitude drop along the capillary was only 0.1% and the phase shift was only 0.2°.

Figure 3(a) shows measurements of p_1 for a typical wave with the loop valve closed to prevent mean flow. The corresponding calculated curves in Figs. 3(a) and 3(b) were generated straightforwardly by integrating the acoustic momentum and continuity equations with DeltaE,[23] using "cone" for each gas diode's tapered portion and "duct" for the rest of the loop. (DeltaE's wall roughness factor for turbulence was set at 5×10^{-4}. Under the conditions of Fig. 3, turbulence is expected in the gas-diodes' cones and near the maxima in volume velocity $|U_1|$ in the 2.21-cm-i.d. pipe, where the gas displacement amplitude over viscous penetration depth is $|\xi_1|/\delta_\nu = 830$ and the Reynolds-number amplitude $|N_{R,1}| = |U_1|\, D_{\rm pipe}\rho_{\rm m}/S_{\rm pipe}\mu = 580\ 000$, where D is diameter, $\rho_{\rm m}$ is mean density, S is cross-sectional area, and μ is viscosity.) An "impedance" at the small end of the cone accounted for the extra dissipation caused by the abrupt area change there, calculated as described near Eq. (19) in Sec. IIIA. To produce the calculated curves in Fig. 3, the mean pressure, temperature, frequency, and the pressure oscillation amplitude in the mixing chamber were fixed at the experimental values. The agreement between the measured and calculated pressure waves in Fig. 3(a) is excellent, inspiring confidence that the calculated wave of volume velocity U_1 is accurate, too. The left–right symmetry in Figs. 3(a) and 3(b) is nearly perfect: The asymmetry of the two gas diodes' orientations has a very small effect on the wave when the valve is closed.

Obtaining meaningful measurements of time-averaged pressure required a multi-step procedure. First, the time-averaged voltages from the pressure transducers were recorded while the apparatus was running in steady state. Next, the power to the drive piston was shut off and a valve was opened to equalize the pressures above and below the piston more quickly than would otherwise have occurred through the leakage around the piston. Time-averaged voltages were again recorded from each transducer, and these were subtracted from the

earlier measurements. This subtraction accounted for different transducers having different offset voltages. These voltage differences were multiplied by the calibration constants of the transducers to yield $p'_{2,0}$ for each transducer. However, these values of $p'_{2,0}$ included a large common-mode effect of no interest to us, due mostly to the front-to-back time-averaged pressure difference across the moving piston, generated in part by nonlinear leakage past the piston. Hence, the common-mode part of $p'_{2,0}$ was eliminated by subtracting $p'_{2,0}$ in the mixing chamber from its value at each of the transducers, yielding $p_{2,0}$. Figure 3(c) shows a typical set of such results, with $p_{2,0} \equiv 0$ in the mixing chamber (at $x = 0$ and $x = 6.33$ m) a consequence of this procedural definition of $p_{2,0}$.

The calculated curve $p_{2,0}(x)$ shown in Fig. 3(c) includes both reversible nonlinear effects and irreversible nonlinear effects. The reversible effects arise from what can be loosely described as the acoustic version of Bernoulli's equation, with low time-averaged pressure at locations of high time-averaged velocity. The well-known lossless expression[24,25] obtained by properly time averaging lossless equations of fluid mechanics,

$$p_{2,0}(x) = \frac{|p_1(x)|^2}{4\rho_{\rm m} a^2} - \frac{\rho_{\rm m} |U_1(x)|^2}{4\ [S(x)]^2} + C, \tag{1}$$

where a is the sound speed, with p_1 and U_1 from Figs. 3(a) and 3(b), was used to compute the smoothly varying portions of the curve of Fig. 3(c). The two steep portions of the solid curve in Fig. 3(c), extending below the bottom of the graph, indicate the contribution of $S(x)$ in the conical tapers of the gas diodes to Eq. (1).

The three abrupt steps in the curve of Fig. 3(c), two (dotted lines) at the small ends of the gas diodes and the third (no line) at the valve, mark changes in the constant C in Eq. (1) from region to region in the apparatus. The small end of each gas diode generates its step in $p_{2,0}$ from a combination of the effect of the step in area in Eq. (1) and the irreversible "minor loss."[26] The algorithm used to calculate the magnitude of the minor-loss contribution is described in Sec. IIIA. The steps in $p_{2,0}$ located at and caused by the gas diodes impose their sum across the valve at $x = 3.2$ m, where the pressure difference of 4 kPa represents the effect that encourages nonzero mean flow as soon as the valve is opened. The experimental values of these irreversible steps shown in Fig. 3(c) are about 10% smaller than the calculated values. Other than this discrepancy, which is examined in more detail in Sec. IIIB, the agreement between the experimental and calculated values in Fig. 3(c) is excellent.

The insulated pipes included type-K thermocouples and electric-resistance heaters with locations as shown in Fig. 2. The 22 thermocouples on the loop itself were spot welded to the outside of the pipe and were approximately equally spaced, except for a larger gap across the valve at the top. Wrapped around the outside of the straight sections of the loop were flexible heaters,[27] with power delivered by a variable autotransformer and measured with an electronic power meter.[28] Surrounding the heaters and all the unheated parts of the loop was a layer of flexible foam insulation, 2 cm thick, of the type often used to insulate residential hot water pipes. Measurements with the heaters and thermocouples and with no acoustics showed that the thermal conductance through this insulation was 2 W/°C, about twice the value estimated from the dimensions and the nominal insulating value "R5," the excess presumably due to imperfections associated with the valve, fittings, pressure transducers, elbows, etc. and the fact that the heaters covered only the convenient long parts of the loop. To reduce this heat leak, an additional layer of rigid fiberglass insulation (of the type often used to cover industrial steam pipes) was added to the straight portions, bringing their total diameter to 11.4 cm, and 3 to 5 cm of soft fiberglass was added around the elbows and valve (including the valve handle). This reduced the measured thermal conductance through the insulation to 1.15 W/°C. Figure 4 shows measurements of the temperature distribution $T(x)$ for three simple circumstances, giving some indication of the variability in local temperatures resulting from spatial nonuniformity in coverage by the electric heaters, acoustic power dissipation, and thermoacoustic heat pumping. With electric heat and no acoustic oscillations, the thermocouples closest to the unheated portions (the gas diodes and the valve) are the coolest. With the most intense acoustic oscillations, the thermocouples near the gas diodes, where dissipation of acoustic power is highest, are the warmest.

Connecting both ends of the loop to the driving system, at the bottom of Fig. 2(a) and shown in more detail in Fig. 2(c), was the "mixing chamber." The mixing chamber was an open cylindrical space 10.2 cm in diameter and 3.18 cm tall, with the loop connections at diametrically opposite locations. In addition to the pressure transducer mounted in its side wall, the mixing chamber contained five thermocouples, extending into the gas itself, axially centered and at various radial and azimuthal positions. A sixth thermocouple extended into the loop 5 cm, on the "hot" side, i.e., the side delivering mean flow from the loop to the mixing chamber.

Water-cooled heat exchangers above and below the mixing chamber, shown in Fig. 2(c), were included when needed to remove heat from the system. Each heat exchanger was a cross-drilled brass block, with 404 holes of 2.26-mm diameter and 20.6-mm length through which the argon oscillated vertically, and 51 perpendicular holes of the same diameter and various lengths up to 10.2 cm through which ambient-temperature water flowed horizontally.

The oscillations in the system were driven by an oscillating piston of 10.16 cm diameter, below the lower heat exchanger. The piston was driven in turn by a linear motor, not shown in Fig. 2. The base plate, piston, and motor came as a complete package from the motor manufacturer,[29] with the motor housing sharing the same gas and mean pressure as the experimental system, so that perfect piston sealing was unnecessary and the gas exerted no significant time-averaged force on the piston.

A mutual-inductance-based linear variable displacement transducer[30] (LVDT) was mounted on the motor to indicate the piston's mean position ξ_{m} and its complex displacement oscillation amplitude ξ_1. The LVDT was electrically excited at 10 kHz and monitored by a lock-in amplifier[21] operating at that frequency. With the lock-in time constant at 3 s, this LVDT–lock-in combination was calibrated in situ by driving the motor with enough dc current (first of one sign, then of the other) so that an opaque edge moving with the piston half blocked the light path of either of two LED–photodiode sets. The known distance between the two LED–photodiode sets and the lock-in readings at the two positions yielded the calibration of the lock-in–LVDT combination. For measurements of ξ_{m}, this lock-in's time constant was kept at 3 s. For measurements of ξ_1, this lock-in's time constant was set at 10 μs, and its output was fed to the input of the lock-in used to measure p_1. With the piston moving at 50 Hz at just the right amplitude, comparison of the LVDT signal with the signals from the photodiodes showed that these measurements of ξ_1 are accurate to 1% in amplitude and 1° in phase.

To establish more confidence in the measurement of ξ_1, we temporarily replaced the loop, mixing chamber, and heat exchangers with the shortest possible 10-cm-diameter cylinder and a dummy load, i.e., a valve functioning as a variable resistance in series with a tank of known volume V. The powers dissipated in the load[31] and delivered by the piston are given

by

$$\dot{E}_{\rm load} \cong \frac{\omega V}{2\gamma p_{\rm m}} {\rm Im}[p_{1,{\rm pist}}\ \widetilde{p}_{1,{\rm tank}}], \tag{2}$$

$$\dot{E}_{\rm pist} = -\frac{\omega S_{\rm pist}}{2} {\rm Im}[p_{1,{\rm pist}}\ \widetilde{\xi}_1], \tag{3}$$

where $\omega = 2\pi f$, f is the drive frequency, γ is the ratio of isobaric to isochoric specific heats and the tilde denotes complex conjugation. Figure 5 shows a comparison of these powers for two different pressure amplitudes as the variable resistance was changed. The fact that the observed slopes on this plot are close to unity confirms the accuracy of the measurements of $\dot{E}_{\rm pist}$ and, hence, of $|\xi_1|$ and the phase between ξ_1 and p_1.

The vertical offsets of the two sets of measurements in Fig. 5 depended on pressure amplitude and were larger than could be accounted for simply by thermal-hysteresis losses on the surface of the short 10-cm-diameter cylinder. We assume that the excess is due to oscillatory leakage past the piston. Measurements of this excess power dissipation as a function of amplitude are fit well by

$$\dot{E}_{\rm leak} = \left(0.00014\ {\rm W/kPa}^{2.25}\right) |p_1|^{2.25}. \tag{4}$$

Some aspects of this leakage dissipation (e.g., the dependence of $\dot{E}_{\rm leak}$ on $|\xi_1|$ and $\xi_{\rm m}$) were not fully explored at the detailed level of a few Watts. Greater care was not justified, because other dissipative effects in the mixing chamber, such as the effect of amplitude-dependent turbulence on the thermal-hysteresis losses on the surfaces of the heat exchangers, are not understood at that level of detail. Overall, we estimate that the measurements of the acoustic power delivered to the mixing chamber by the piston have an uncertainty of about 2% due to sensor-calibration uncertainties plus a few Watts due to this leakage dissipation.

During the course of the measurements, with temperature often a significant function of location x around the loop and with mean flow often nonzero, an easy experimental definition of loop resonance was needed so that the drive frequency could be chosen without having to map out the entire wave as shown in Fig. 3(a). We decided to use the condition

$${\rm Re}[\xi_1/p_{1,{\rm pist}}] = 20\ \mu{\rm m/kPa} \tag{5}$$

to define resonance, where $p_{1,{\rm pist}}$ is the complex pressure oscillation amplitude above the piston and the numerical value of 20 μm/kPa is obtained from the calculated compliance

of the mixing chamber, heat exchangers, and adjacent 10-cm-diam spaces in the driver assembly. The numerical value varied slightly with amplitude, because $\xi_{\rm m}$ varied slightly. For left–right symmetry in the loop, Eq. (5) implies that the impedances of both branches from the mixing chamber to the loop are real, an unambiguous definition of loop resonance frequency. For more general, asymmetrical conditions, Eq. (5) implies that the sum of the imaginary parts of the inverse impedances of the two branches is zero, so that if one end of the loop looks inertial the other must look compliant. Before recording any other data, measurements of ξ_1 and $p_{1,\rm pist}$ were obtained, $\mathrm{Re}[\xi_1/p_{1,\rm pist}]$ was computed, f was adjusted, and the process was repeated until Eq. (5) was satisfied. This typically took only a minute to reach a resonance frequency precise to ± 0.01 Hz. However, the accuracy of the resonance frequency determined in this way was in doubt ± 0.5 Hz. The numerical value used in Eq. (5) was uncertain because of uncertainty in how much of the calculated compliance volume, which included the heat-exchanger passages, should be regarded as isothermal instead of adiabatic. The more accurately known value of 17.4 μm/kPa was used for measurements when the heat exchangers were omitted.

With the water-cooled pipes in use, the experimental resonance frequency defined in this way decreased when the valve was opened at fixed acoustic amplitude. The decrease varied from 0.5% at low amplitude to 0.7% at high amplitude. Most of this change can be attributed to the 0.4% increase in length of the loop as the passage inside the "ball" of the valve became part of the acoustic path. The experimental resonance frequency increased quadratically with acoustic amplitude, by 0.6% from low amplitude to $|p_1| = 240$ kPa when the valve was closed and by 0.8% when the valve was open. How much of this rise is attributable to temperature rise in the gas is unknown. Note that about a third of the acoustic power dissipation in the loop occurs in the gas diodes, which are at velocity maxima of the wave where a change in temperature has the largest effect on the resonance frequency.

In the calculations plotted in Fig. 3 and throughout the rest of the paper, the experimental frequency was used in the calculations. Forcing the calculations to mimic the experimentally defined resonance (i.e., to zero the sum of the calculated imaginary parts of the impedances of the two ends of the loop at the mixing chamber) could be accomplished either by setting the calculation's frequency 1% above the experimental resonance frequency or be reducing the calculation's temperature by 2% to reduce the sound speed by 1%. However, this alternative

calculation scheme made little difference in other calculated results.

III. CIRCULATING MEAN FLOW

A. Theory

In Fig. 3(c), the step in $p_{2,0}$ across the valve shows that the loop is ready to deliver nonzero time-averaged mass flow $\dot{M}$ in the positive-x direction as soon as the valve is opened.[22] In this subsection, analysis directed toward understanding such time-averaged effects is presented. This analysis is based on simple assumptions, but nonetheless captures many of the experimental features described below. The quasi-steady approximation is central: We proceed as if the results of steady-flow analysis can be applied at each instant of time without memory of recent past history.

The irreversible part of the turbulent-flow pressure difference δp across any lumped element, including minor-loss components such as gas diodes, is conventionally[32] expressed using the minor-loss coefficient K :

$$\delta p = K\rho u^2/2, \tag{6}$$

where ρ is the gas's density and u is its velocity at a reference location in the lumped element. Hence, for superimposed steady and oscillatory flows the irreversible part of the time-averaged pressure difference developed across each component due to the time-dependent flow through it can be estimated using

$$\delta p = \frac{\omega}{2\pi}\oint_0^{2\pi/\omega} \delta p(t)\, dt \tag{7}$$

$$= \frac{\omega}{2\pi S^2}\left[\int_{t_0}^{\pi/\omega - t_0} K_+ \frac{1}{2}\rho\left(|U_1|\sin\omega t + \dot{M}/\rho\right)^2 dt - \int_{\pi/\omega - t_0}^{2\pi/\omega + t_0} K_- \frac{1}{2}\rho\left(|U_1|\sin\omega t + \dot{M}/\rho\right)^2 dt\right], \tag{8}$$

where K_+ and K_- are the minor-loss coefficients for the two directions of flow through the component, S is the area on which the K's are based (conventionally, the smallest cross-sectional area of the component), t is time, and t_0 is the time at which the volume velocity crosses zero, i.e., t_0 satisfies $|U_1|\sin\omega t_0 + \dot{M}/\rho = 0$. (If $\left|\dot{M}/\rho\right| > |U_1|$, no solution for t_0

exists, and either the K_+ or K_- integral is carried out from 0 to $2\pi/\omega$. Otherwise, the zero crossing with $-\pi/2 < \omega t_0 < 0$ is chosen if $\dot{M} > 0$.) Equation (8) is a straightforward extension of the discussion near Eq. (7.76) in Ref. 33.

Our choice of notation for the steady flow calls for some explanation, because no choice seems completely satisfactory. Results below show that $\dot{M}$ is approximately proportional to the first power of the amplitude of the wave and is comparable in size to $\rho_{\rm m} |U_1|$, but a subscript "1" would be misleading because it would improperly suggest that $\dot{M}$ is complex or oscillatory. A subscript "m" would inappropriately suggest that this steady flow exists in the absence of the sound wave (just as $p_{\rm m}$ and $\rho_{\rm m}$ exist in the absence of the wave). We have chosen to use $\dot{M}$, without subscripts, because it is simple and because the most reliable measurements described below detect mass flow, not volume flow. The mass flow $\dot{M}$ in this paper should not be confused with the much smaller, second-order time-averaged mass flow $\dot{M}_2 = \frac{1}{2}{\rm Re}[\rho_1 \widetilde{U}_1] + \rho_{\rm m} U_{2,0}$ in previous work.[10,11,33]

Assuming that all variables except t itself are independent of time, performing the integrals in Eq. (8) yields the irreversible second-order time-averaged pressure difference

$$\delta p_{2,0} = -K_- \left(\dot{M}^2 / 2\rho_{\rm m} S^2 + \rho_{\rm m} |U_1|^2 / 4S^2 \right) \text{ for } \varepsilon \le -1, \tag{9}$$

$$= \frac{\rho_{\rm m} |U_1|^2}{8S^2} (K_+ - K_-) \times \left\{ 1 + 2\varepsilon^2 + \frac{K_+ + K_-}{K_+ - K_-} \frac{2}{\pi} \left[\left(1 + 2\varepsilon^2\right) \sin^{-1} \varepsilon + 3\varepsilon \sqrt{1 - \varepsilon^2} \right] \right\} \text{ for } |\varepsilon| \le 1, \tag{10}$$

$$= K_+ \left(\dot{M}^2 / 2\rho_{\rm m} S^2 + \rho_{\rm m} |U_1|^2 / 4S^2 \right) \text{ for } \varepsilon \ge 1, \tag{11}$$

where the flow-rate ratio $\varepsilon = \dot{M} / \rho_{\rm m} |U_1|$. Our gas diodes operate with $|\varepsilon| < 1$, so that the flow passes through zero twice during each cycle. When $|\varepsilon| > 1$, the flow is unidirectional. Signs have been chosen so that positive δp discourages positive $\dot{M}$ and K_+ corresponds to flow in the $+x$ direction.

To obtain $\delta p_{2,0}^{\rm gd}$ for our gas diodes' geometry from Eq. (10), we use the well-established Borda-Carnot expression[34]

$$K_- = (1 - S_{\rm gd}/S_{\rm pipe})^2 \tag{12}$$

for minor-loss flow through the abrupt expansion from $S_{\rm gd}$ to $S_{\rm pipe}$ to obtain $K_- = 0.364$. We combine equations and a chart from Ref. 32, for an abrupt contraction with a rounded edge plus a term accounting for radial nonuniformity in a short conical expander, to obtain

$K_+ = 0.04$. These quasi-steady estimates and the entire quasi-steady approach introduced in Eq. (8) should be accurate for oscillatory flow if the Reynolds number is sufficiently high and if the gas displacement is sufficiently large. For the conditions of Fig. 3, $|N_{R,1,\mathrm{gd}}| = |U_1|\, D_{\mathrm{gd}}\rho/S_{\mathrm{gd}}\mu = 920\ 000$, but $|\xi_1|\,/D_{\mathrm{gd}}$ is only 9, the latter condition perhaps not extreme enough for complete confidence in the quasi-steady approximation.[35,36]

Equations (9)–(11) with $K_+ = K_-$ still depend on ε, so apparently the oscillatory flow affects the time-averaged pressure drop across *symmetrical* turbulent components as well as across the asymmetrical gas diodes. Setting $K_+ = K_- \equiv K$ in Eqs. (9)–(11) yields

$$|\delta p_{2,0}| \;=\; K\frac{\rho_{\mathrm{m}}}{2}\left(\frac{\dot{M}/\rho_{\mathrm{m}}}{S_{\mathrm{pipe}}}\right)^2\left(1+\frac{1}{2\varepsilon^2}\right) \;\text{ for }\; |\varepsilon| \geq 1, \tag{13}$$

$$\;=\; K\frac{\rho_{\mathrm{m}}}{2}\left(\frac{\dot{M}/\rho_{\mathrm{m}}}{S_{\mathrm{pipe}}}\right)^2\frac{\left[(1+2\varepsilon^2)\sin^{-1}|\varepsilon| + 3\,|\varepsilon|\sqrt{1-\varepsilon^2}\right]}{\pi\varepsilon^2} \;\text{ for }\; |\varepsilon| \leq 1. \tag{14}$$

This multiplicative enhancement of the steady-flow pressure drop across a symmetrical turbulent component grows from near unity at small $|U_1|$ though 3/2 at $|U_1| = \dot{M}/\rho_{\mathrm{m}}$ toward a linear asymptote of $4\rho_{\mathrm{m}}\,|U_1|\,/\pi\dot{M}$ at large $|U_1|$. The origin of this increase is the fundamentally nonlinear nature of turbulent flow resistance: If the flow is described by $\delta p(t) = R[U(t)]^n$ with $n \neq 1$, then the extra pressure difference caused by an increment $+\Delta\dot{M}$ of mass flow above the average value $\dot{M}$ is not canceled when an equal decrement $-\Delta\dot{M}$ below the average occurs half a cycle later.

In the loop under investigation here, opposing the pressure differences of Eq. (10) that are generated at the two gas diodes is the time-averaged pressure gradient throughout the rest of the loop due to $\dot{M}$ flowing around the loop. To estimate this pressure gradient, one might expect[37] that standard equations of fluid mechanics, such as

$$\frac{dp}{dx} = -f_M\frac{\rho_{\mathrm{m}}}{2D_{\mathrm{pipe}}}\left(\frac{\dot{M}/\rho_{\mathrm{m}}}{S_{\mathrm{pipe}}}\right)^2, \tag{15}$$

could be used for the mean flow through the uniform-area parts of the loop, where D_{pipe} is the pipe diameter and f_M is the Moody friction factor, which is given in most fluid mechanics textbooks (e.g., Ref. 26). Some of the calculated curves presented below rely on this simple treatment of the mean flow in the loop. However, Eq. (15) describes nonlinear, turbulent flow, so the arguments presented in the previous paragraph suggest that Eq. (15) could significantly underestimate the mean-flow resistance when oscillatory flow is superimposed. Furthermore, the Moody friction factor f_M depends on velocity, so the constant-K

analysis leading to Eqs. (13) and (14) is not suitable. The Appendix presents a derivation of expressions similar to Eqs. (13) and (14) taking the velocity dependence of f_M into account; the result is Eqs. (A.9) and (A.10).

To Eq. (15) or Eqs. (A.9) and (A.10) for the time-averaged pressure gradient along the uniform-diameter portions of the pipe are added two pressure drops due to drag on the mean flow by the conical surfaces of the two gas diodes,[32,38] four pressure drops due to steady-flow minor loss corrections in the four 90° elbows,[34] and one pressure drop due to steady-flow minor loss at the exit from the pipe to the mixing chamber; all of these may also be increased by nonzero $|U_1|$ according to the multiplicative enhancement of Eqs. (13) and (14). These seven pressure drops typically summed to about 50% of that of the uniform-diameter portions.

Setting the sum of the forcing pressures of the two gas diodes equal to the sum of all these opposing steady-flow pressure drops allows one to find $\dot{M}$. This must be done numerically because of the complicated nature of the equations. Qualitatively, Eq. (10) shows that $\delta p_{2,0}^{\mathrm{gd}}$ is proportional to the square of the wave amplitude and Eq. (15) shows that the opposing pressure gradient in the loop is nearly proportional to the square of the mean flow, so one can expect that the mean flow is roughly proportional to the wave amplitude.

Again using the quasi-steady approximation, the acoustic power consumed by a turbulent lumped element such as a gas diode due to the oscillatory component of the flow through it can be estimated using[39]

$$\Delta\dot{E} = \frac{\omega}{2\pi}\oint_0^{2\pi/\omega} \delta p(t)\ |U_1|\sin\omega t\,dt \tag{16}$$

$$= \frac{\omega}{2\pi S^2}\left[\int_{t_0}^{\pi/\omega-t_0} K_+\frac{1}{2}\rho\left(|U_1|\sin\omega t + \dot{M}/\rho\right)^2|U_1|\sin\omega t\,dt \right.$$

$$\left. - \int_{\pi/\omega-t_0}^{2\pi/\omega+t_0} K_-\frac{1}{2}\rho\left(|U_1|\sin\omega t + \dot{M}/\rho\right)^2|U_1|\sin\omega t\,dt\right]. \tag{17}$$

This is a straightforward extension of the discussion near Eq. (7.77) in Ref. 33. Again assuming that variables other than t itself are independent of time, performing the integrals

yields[39]

$$\Delta\dot{E} = -\varepsilon K_- \frac{\rho_m |U_1|^3}{2S^2} \text{ for } \varepsilon \le -1, \tag{18}$$

$$= \frac{\rho_m |U_1|^3}{3\pi S^2} (K_- + K_+) \times \left[\left(1 + \frac{\varepsilon^2}{2}\right) \sqrt{1-\varepsilon^2} + \frac{3}{2}\varepsilon \sin^{-1}\varepsilon - \frac{K_- - K_+}{K_- + K_+} \frac{3\pi\varepsilon}{4} \right] \text{ for } |\varepsilon| \le 1, \tag{19}$$

$$= \varepsilon K_+ \frac{\rho_m |U_1|^3}{2S^2} \text{ for } \varepsilon \ge 1. \tag{20}$$

We then use $\delta p_1 = 2\ \Delta\dot{E}/|U_1|$ as an estimate of the first-order pressure difference caused by irreversible processes in such components.

As in Eqs. (9) and (10), note the nontrivial ε dependence in Eqs. (18)–(20), even if $K_+ = K_-$, indicating that acoustic-power dissipation in a *symmetrical* turbulent component is increased by superimposed steady flow. This increase is given by a multiplicative factor,

$$\left(1 + \frac{\varepsilon^2}{2}\right) \sqrt{1-\varepsilon^2} + \frac{3}{2}\varepsilon \sin^{-1}\varepsilon \text{ for } |\varepsilon| \le 1, \tag{21}$$

$$\frac{3\pi}{4} |\varepsilon| \text{ for } |\varepsilon| \ge 1, \tag{22}$$

if the component's K is independent of velocity. The Moody friction factor f_M depends on velocity, so a more complicated analysis must be used to estimate the dissipation of acoustic power in the straight portions of the pipe in the presence of superimposed steady flow. The Appendix presents a derivation of expressions similar to Eqs. (18)–(20) taking the velocity dependence of f_M into account; the result is Eqs. (A.11) and (A.12).

B. Experiments with nonzero mean flow

To quantitatively test for $\dot{M} \neq 0$ as predicted in the previous subsection, we operated the loop with the valve open. The effect of the mean flow on wave shape and $p_{2,0}$ provided indirect measurements of $\dot{M}$, and the heat carried by $\dot{M}$ provided a nearly direct measure. The water-cooled pipes were most convenient for measurements of wave shape and $p_{2,0}$, because rapid equilibration to steady state enabled rapid data taking and because the spatial uniformity of temperature yielded more confidence in calculations of the wave. Measurements with the heated and insulated pipes were used to detect heat carried by $\dot{M}$.

With the valve open, the loop has the topology of a constricted annular resonator driven at one point, whose complicated behavior has been described by Muehleisen and Atchley.[40] Without constrictions or dissipation, the modes of such a resonator are degenerate: With the length of the loop equal to one wavelength, standing waves of any spatial phase and traveling waves of either direction satisfy the wave equation and share a single resonance frequency. Reference 40 shows that area constrictions eliminate the degeneracy, splitting the resonance into a "high" standing-wave mode and a "low" standing-wave mode. In the low mode, a velocity antinode is centered on the constriction, so the resonance frequency is reduced because of the increased inertance of the constriction. In the high mode, a pressure antinode is centered on the constriction, so the resonance frequency is increased by the reduced compliance of the constriction. In the present experiment, the gas diodes are constrictions, and the low mode is desired. The resonance condition described near Eq. (5) selects the low mode. Only 2 Hz higher in frequency, a weak local maximum in $|p_1|$ at the gas diodes suggests the presence of the high mode.

The steps at the gas diodes in the calculated curves for $\mathrm{Im}[p_1]$ and $p_{2,0}$ in Figs. 3(a) and 3(c) are based on Eqs. (19) and (10), respectively, with $S = S_{\mathrm{gd}}$ and $\dot{M} = 0$. These steps, and all other features of the curves, are in qualitative agreement with the measured pressures. Figure 6 shows corresponding measurements and calculations for $\dot{M} \neq 0$, with the valve open at the top of the loop. The overall character of the wave is still that of a standing wave, as indicated by the cosine shape of $\mathrm{Re}[p_1]$ in Fig. 6(a), for which measured and calculated values are in good agreement. However, $\mathrm{Im}[p_1]$ changed dramatically when the valve was opened.

The solid lines in Figs. 6(a) and 6(b) represent the results of calculations using DeltaE, as described near the beginning of Sec. II and with the steady-flow phenomena calculated assuming that the mean and oscillatory components of the velocity are independent except at the gas diodes where they are linked through Eqs. (10) and (19). The dramatic disagreement between the experimental $\mathrm{Im}[p_1]$ and this calculation motivated us instead to model the Doppler effects (for which DeltaE cannot yet account) of opposite signs in the nearly equal counterpropagating traveling-wave components of the standing wave. In the Doppler model,

implemented in a spreadsheet, we used

$$p_1 = Ae^{-ik_+x} + Be^{ik_-x}, \tag{23}$$

$$U_1 = \frac{iS}{\omega\rho_{\rm m}}\left(1 + im\frac{2\delta_\nu}{D}\right)\left(-ik_+A\ e^{-ik_+x} + ik_-B\ e^{ik_-x}\right), \tag{24}$$

$$k_\pm = \frac{\omega}{a \pm \dot{M}/\rho S}\left(1 - im\frac{[\delta_\nu + (\gamma-1)\,\delta_\kappa]}{D}\right), \tag{25}$$

where $k_\pm$ are the wave vectors for waves traveling with and against[41] the mean flow, A and B are the pressure amplitudes of those waves, δ_κ is the thermal penetration depth, and $i = \sqrt{-1}$. With $[\delta_\nu + (\gamma-1)\,\delta_\kappa]\,/D_{\rm pipe} = 0.005$, the boundary-layer approximation used in Eqs. (23)–(25) is well justified. In the spreadsheet, the turbulence correction factor m is calculated according to the algorithm used in DeltaE[23] and described near Eq. (7.26) in Ref. 33, but with an additional correction due to the superimposed steady flow given in Eqs. (A.15) and (A.16). For laminar flow, $m = 1$; for turbulent flow, $m > 1$. In the Doppler-model spreadsheet, each of the four long runs of pipe was subdivided into eight pieces, and each gas-diode cone into two pieces; further subdivision did not change the results. Equations (23) and (24) were used for wave propagation in each such piece, with continuity of p_1 and U_1 joining solutions between pieces. As in the DeltaE calculation, Eq. (19) was used for the minor-loss contribution to δp_1 across the gas diodes and Eqs. (10), (A.10), and the discussion in the paragraph following Eq. (15) were used to obtain $\dot{M}$. Complex U_1 at $x = 0$ was used as an adjustable parameter to ensure that complex $p_1(0) = p_1(6.33\ {\rm m})$. The calculation's gas temperature, which was constant along the pipe, could also be adjusted slightly above the experimental value to enforce ${\rm Im}[U_1(0)] = {\rm Im}[U_1(6.33\ {\rm m})]$, corresponding to our operational definition of resonance, but this adjustment had a negligible effect. The result, shown as the dashed lines in Fig. 6(a) and (b), displays ${\rm Re}[p_1]$ and ${\rm Im}[p_1]$ in agreement with the experimental values. The agreement between this calculation and the measurements strongly suggests that the Doppler effect is primarily responsible for the large values of ${\rm Im}[p_1]$.

To consider this effect in more detail, notice that the measured ${\rm Im}[p_1]$ in Fig. 6(a) is not left–right antisymmetric; the depth of the minimum near $x = 4.8$ m exceeds the height of the maximum near $x = 1.6$ m. This downward shift resembles that of the $\dot{M} = 0$ data in Fig. 3(a), where ${\rm Im}[p_1] < 0$ is associated with the flow of acoustic power into the loop from both ends. To more clearly distinguish the effect of $\dot{M} \neq 0$ from that of the acoustic power flow, in Fig. 7 we display the difference between $\dot{M} \neq 0$ and $\dot{M} = 0$ measurements of ${\rm Im}[p_1]$ at the

four pressure transducers closest to the two gas diodes, at five different pressure amplitudes. The subtraction brings the results at the four transducers into agreement with one another, and plotting these against the 3/2 power of the wave amplitude yields a reasonably straight line. We do not understand why $\dot{M} \neq 0$ should contribute to $\mathrm{Im}[p_1]$ in proportion to the 3/2 power of the wave amplitude.

Our spreadsheet-based Doppler calculations, also displayed in Fig. 7, show the difference between $\mathrm{Im}[p_1]$ when $\dot{M} \neq 0$ and $\dot{M} = 0$ more nearly proportional to the square of the wave amplitude. The difference between calculated and measured $\mathrm{Im}[p_1]$ in Fig. 7 might simply be due to $\dot{M}$ depending on physics that we do not understand. However, one other candidate is apparent: Both the calculations and the measurements for $\dot{M} \neq 0$ displayed a remarkably strong dependence of $\mathrm{Im}[p_1]$ on frequency as frequency was changed away from resonance. Both rose with frequency; measured values rose about 30% per Hz and calculated values about 40% per Hz. Hence, some of the difference between calculations and measurements in Fig. 7 could be a small amplitude-dependent error or ambiguity about what really constitutes resonance frequency or what gas temperature should be used in the calculations.

With such an imperfect understanding of $\mathrm{Im}[p_1]$, we cannot be confident in the accuracy of $\mathrm{Re}[U_1]$ in Fig. 6(b). However, $\mathrm{Re}[p_1]$ appears to be well understood, and hence we should have confidence in the calculation of $\mathrm{Im}[U_1] \propto d\,\mathrm{Re}[p_1]/dx$, which is the dominant part of the volume-velocity wave. The time-averaged pressure difference across the gas diodes and the resulting mean flow are due to $|U_1|^2$ at the gas diodes, where $\mathrm{Re}[U_1]$ is negligible.

Hence, uncertainty about $\mathrm{Im}[p_1]$ in Fig. 6(a) has a negligible effect on the calculated curve for $p_{2,0}$ in Fig. 6(c). The measured and calculated values of $p_{2,0}$ are in reasonable agreement. Table I shows the magnitudes of various contributions to the calculated curve. As in Fig. 3(c), the largest contributor is the reversible effect expressed by Eq. (1), so the agreement between measurements and calculations in that aspect of Fig. 6(c) strengthens confidence in our knowledge of $|U_1|$. The steps in $p_{2,0}$ at the gas diodes are smaller than they were in Fig. 3(c), reflecting the ε dependence in Eq. (10). The measured steps at the gas diodes appear significantly smaller than the calculations.

Closer examination of the time-averaged pressure difference across the gas diodes was challenging. Initially, the transducers closest to the gas diodes were simply installed in the

pipes with their tips retracted slightly from the pipe inner surface, as suggested in Ref. 42. The most linear transducers were selected from our inventory, so that time-averaged voltage would have no significant contribution from oscillating pressure interacting with transducer nonlinearity;[42] we estimate that this effect is less than 10 Pa for any conditions encountered in these measurements. Nevertheless, following the measurement procedure described just above Eq. (1) and swapping transducers from place to place showed systematic errors as large as 0.7 kPa. We suspected that the temperature dependence of the transducers' offset voltages might be responsible, because the sensing element of the transducer might be at one temperature when the sound was on and another when it was off. Hence, we separated the transducers from the pipe by the 4-cm capillaries described in Sec. II. (The end-to-end time-averaged pressure difference in each capillary, due to nonlinear acoustics in the capillary and minor losses at its ends,[42] is estimated to be < 5 Pa.) We also reduced the transducer bias voltage to 2.5 V instead of the manufacturer's recommended 10 V in a further attempt to keep the transducers near room temperature whether the sound wave was on or off. From among our most linear transducers, we also selected two with the lowest offset-voltage temperature dependence and used them for all measurements. Despite these efforts, swapping transducers from place to place and repeating experimental conditions suggests that a systematic error up to 0.2 kPa remains. (Random uncertainty associated with reading the voltmeter is ~ 0.1 kPa.)

With all these instrumental precautions, measurements of the time-averaged pressure differences across the gas diodes are shown in Fig. 8 as a function of the square of the wave amplitude. Filled symbols represent measurements with the valve closed; open symbols, the valve open. Pairs of data with the same symbols indicate a top-to-bottom interchange of the transducers, all other conditions being equal, displaying a lower bound of ~ 0.2 kPa on the remaining systematic uncertainty in the measurements.

The line in Fig. 8 corresponding to the $\dot{M} = 0$ measurements was calculated using Eq. (10). The line corresponding to the $\dot{M} \neq 0$ measurements is the calculated value of $\delta p_{2,0}$ between the pressure transducers nearest to the gas diode, which is mostly due to Eq. (10) but with a typically 20% contribution from the flow impedance of the cone. The quadratic dependence of $\delta p_{2,0}$ on $|p_1|^2$ in Fig. 8 corresponds to the quadratic dependence of $\delta p_{2,0}$ on $|U_1|^2$ in Eq. (10). However, the experimental magnitudes are significantly less

than those predicted by Eq. (10) with the values for K_- and K_+ given below Eq. (11). Distracted for weeks by systematic errors arising from transducer imperfections, we did not at first recognize that this significant disagreement probably arises from an important hydrodynamic phenomenon. The time-averaged pressure change across the small end of each diode, indicated by the dotted vertical line segments in Figs. 3(c) and 6(c), is not sharply localized at the end of the diode. The pressure transducer 4.8 cm from the small end of the diode is actually located within the pressure-change zone. Subsequent measurements with the transducer 1.3 cm from the small end of the diode yielded measured $\delta p_{2,0}$ almost twice as large, and moving the transducer to 8.3 cm away from the end of the diode reduced the measured $\delta p_{2,0}$ significantly. This entire range of locations is probably within the zone of vortex formation, lateral spatial nonuniformity, and pressure recovery when the gas flows out of the small end of the diode, because these locations are within the gas stroke lengths $2\left|U_1\right|/\omega S_{\rm gd} = 25$ cm and $2\left|U_1\right|/\omega S_{\rm pipe} = 10$ cm.

Tentative conclusions can be drawn from Fig. 8 despite these uncertainties. The time-averaged pressure difference across the gas diodes is smaller with the valve open than with the valve closed, corresponding to the calculated reduction arising from $\varepsilon \neq 0$ in Eq. (10). The measured and calculated closed–open differences are in quantitative agreement, suggesting that the measured closed–open pressure difference might be a useful, quantitative measure of $\dot{M} \neq 0$ via the ε dependence in Eq. (10). However, the gas diode near $x = 4.8$ m was always stronger than the diode near $x = 1.6$ m. Swapping diodes, pipes, and/or transducers indicated that this phenomenon was not an artifact of hardware imperfections; it was associated with the diodes' locations and orientations in the acoustic wave. This is evidence of behavior beyond the quasi-steady approximation.

While Figs. 7 and 8 show indirect, pressure-based evidence of nonzero mass flow around the loop when the valve is open, temperature-based measurements such as shown in Fig. 6(d) provide direct evidence. Figure 6(d) shows typical appearances of measurements of temperature as a function of position around the loop with $\dot{M} \neq 0$. The temperature rises as the gas moves around the loop in the positive-x direction, receiving more and more heat from the electric heaters and from dissipation of acoustic power. For the erect triangles, two curves roughly illustrate the physics that we believe is most important for the appearance of the data. The dashed curve shows a rough estimate of the gas temperature as a function

of x. Its slope is nonzero in the four electrically heated regions of the loop and is zero in the unheated regions near the ends of the loop, the valve, and the gas diodes. However, the measurements of temperature were made on the metal pipe, not in the gas; the difference between the pipe and gas temperatures must be proportional to the local rate of heat transfer from pipe to gas and inversely proportional to the local pipe-to-gas heat-transfer coefficient. The solid curve in Fig. 6(d) shows a rough estimate of the pipe temperature, calculated using a Nusselt number[14] of $0.02\,[N_R(x)]^{0.8}$, with the Reynolds number N_R based on the square root of the sum of the squares of the mean velocity and the x-dependent rms oscillatory velocity. This rough estimate seems to capture the main qualititative features of the data, presumably because the heat-transfer coefficient is highest near the gas diodes where the oscillatory velocity is highest.

The symbols in Fig. 9 represent steady flows inferred from data such as those in Fig. 6(d), independent of the details of the pipe-to-gas heat-transfer model. These mass flows are obtained from $\dot{Q} = \dot{M} c_p \Delta T$, where $c_p = 520$ J/kg-°C is the isobaric specific heat of argon and $\dot{Q}$ and ΔT are heat input and temperature rise obtained from measurements. $\dot{Q}$ is the electric power applied to the loop, minus an estimate of the heat leak through the insulation, plus an estimate of the acoustic power dissipated in the loop. The heat-leak correction varied from 8% to 20% for most of the data, but was 25% and 38% for the points at 50 and 25 kPa, respectively. The acoustic-power correction varied from 1% at the lowest amplitude through 10–20% in the middle amplitudes to 30% and 60% for the measurements at 227 kPa and 238 kPa, respectively. This correction used the measured piston power, with an estimate of the small dissipation due to blowby and heat-exchanger impedance subtracted. The circles in Fig. 9 represent measurements with the loop average temperature in the range 43–47 °C and the temperature rise around the loop in the range 13–17 °C. The triangles represent measurements with higher heats and temperatures, with the loop average temperature in the range 57–60 °C and the temperature rise around the loop in the range 20–24 °C. Hence, the acoustic-power correction was a much larger fraction of the total power for the circles than for the triangles, and the fact that these two sets of measurements are well aligned in Fig. 9 indicates that the acoustic-power correction is not unreasonable. The open symbols in Fig. 9 are based on the full power as described above and the full temperature rise around the loop from $x = 0.14$ m to $x = 6.19$ m, using thermocouples that were not on the electrically heated

portions of the loop. The filled symbols are based on half of the power and a temperature rise equal to the difference between the average temperature of thermocouples in the range 3.5 m $\leq x \leq$ 6.1 m and those in the range 0.3 m $\leq x \leq$ 2.8 m. The highest measured mass flow is 50 gm/s. The total mass of argon in the loop is only 95 gm, so the mean flow clears the entire loop every two seconds at the highest acoustic amplitude.

The two lines in Fig. 9 are two attempts to model the mass flow as a function of amplitude. The solid line represents the results of calculations assuming that the mean flow and the acoustic oscillations are independent, except at the gas diodes where Eq. (10) couples them. The resistance of the loop to mean flow is calculated using Eq. (15), a similar expression for the cone resistance, and small additions for the elbows and the mixing-chamber entrance. Thus, the solid line corresponds to the solid curves in Fig. 6. This calculation overestimates the mean flow, so it must overestimate the strength of the diodes or underestimate the mean-flow resistance of the rest of the loop. The dashed curve represents calculations also using Eq. (10) for the gas diodes but taking more complicated interactions between the steady and oscillating flows into account elsewhere, including the Doppler effect of the mean flow on the oscillations and the enhancement of the mean-flow resistance by the oscillations as described in the Appendix. This calculation underestimates the mean flow, so it is likely that the derivation in the Appendix overestimates the effect of the oscillations on the mean-flow resistance.

C. Acoustic power consumption

Measurements of the acoustic power delivered by the piston, $\dot{E}_{\rm pist}$, are shown in Fig. 10. The data are plotted as a function of the cube of the pressure amplitude, because Eq. (19) indicates that the acoustic power consumed by the diodes is proportional to the cube of the volume-velocity amplitude and the turbulent dissipation of acoustic power in the pipes, as in Eqs. (A.11) and (A.12), would be proportional to the cube of the volume-velocity amplitude if f_M were independent of velocity. The data fall on a curve that is slightly concave downwards, indicating a dependence on amplitude slightly weaker than the cubic. Measured piston power with $\dot{M} = 0$ is indicated by the inverted triangles, and $\dot{M} \neq 0$ is indicated by the erect triangles.

Two sets of curves in Fig. 10 represent the results of calculations using the Doppler

mathematics with Eq. (19) for the dissipation of acoustic power by the diodes and Eqs. (A.11) and (A.12) for the dissipation of acoustic power in the pipes. Although the total calculated power is in reasonable agreement with the measured power, the calculations show a significant difference in piston power between $\dot{M} = 0$ and $\dot{M} \neq 0$ that was not observed. The difference in the calculated values arises from the dependence of Eq. (19) on $\dot{M}$; the diode should require less acoustic power when $\dot{M} \neq 0$. We do not understand why this difference does not appear in the measurements.

It is natural to consider the efficiency of an isolated gas diode as a pump. The power that it delivers to the mean flow is $\delta p_{2,0}^{\mathrm{gd}} \dot{M}/\rho_{\mathrm{m}}$, while the power it consumes is $\Delta \dot{E}_{\mathrm{gd}}$. The ratio of these, obtained from Eqs. (10) and (19), is the efficiency of the pump itself, shown in Fig. 11. (The efficiency of the entire circulating system, where the heat-transfer surface area necessarily consumes additional acoustic power, is lower.) Equations (10) and (19) show that the pump efficiency is a function only of ε and of $\beta = (K_- - K_+)/(K_- + K_+)$. For the experiments described here, $\varepsilon \sim 0.2$ and $\beta = 0.80$, so the efficiency is only about 10%. It seems likely that gas diodes with β as high as about 0.90 are possible, yielding efficiencies as high as 20%.

Figure 11 indicates the importance of working near the optimal ε. For a given, desired $\dot{M}$ and a given $|p_1|$ at the trunk, this specifies the pipe area. Minimizing mean-flow and acoustic losses then suggests a single pipe with circular cross section. If the pipe area is large, the gas diode itself can consist of a plate with many conical holes in parallel, so that their taper angle can remain narrow while their length is short. Considerations of heat-transfer surface area and acoustic techniques to minimize dissipation[43] may call for x-dependent cross-sectional area along the pipe and for subdivision of parts of the loop into several parallel pipes.

IV. CONCLUSIONS

Gas diodes properly located in a resonant loop of piping can cause a substantial mean flow, which in turn can carry substantial heat. For example, near $\dot{M} = 50$ gm/s this loop carried 400 W of heat from the electric heaters to the mixing chamber, the gas temperature rising only 25 °C along the circumference of the loop. Helium is more commonly used than argon in thermoacoustic and Stirling engines and refrigerators. Straightforward similitude scaling[44] of the 50-gm/s operating point to a 3-MPa, 80-Hz helium loop with total length

12.6 m and pipe diameter 4.4 cm shows that with the same temperature profile it would carry 6 kW, an order of magnitude that is of interest for many potential applications.

Whether this concept will find use in such applications will depend in part on economic trade-offs between the low fabrication costs and high reliability of this design and the lower acoustic power consumption of traditional heat exchangers. However, engineering design based on the ideas presented here is already showing ways to reduce the acoustic power consumption without compromising simplicity.[45]

The steady flow created by gas diodes in a resonant loop can be detected by its effect on the acoustic wave and on time-average pressure, as well as by the heat that it carries. The quasi-steady approximation yields results in rough agreement with such measurements. However, many interesting fundamental questions and areas for further research remain. The mutual influence of turbulent mean and oscillatory flows is a theoretical and experimental challenge; the quasi-steady approximation used here is clearly inadequate. Near the diodes, dense arrays of better pressure transducers will illuminate interesting physics of vortex rollup, dissipation, and pressure recovery at the small end of the diode and will answer very basic questions such as what angle suffices to prevent separation in the cone for flow out of the large end of the diode. Also, details of the three-dimensional mean and oscillatory velocity fields in the mixing chamber, and the associated dependence of temperature on position and time, promise to be very interesting to explore and to understand in a way that leads to uniform heat transfer to or from the face of a stack or regenerator.

Acknowledgments

This work was supported by OBES/DMS in the US Department of Energy's Office of Science. We thank Barton Smith and Konstantin Matveev for helpful conversations and David Gardner for practical contributions.

APPENDIX: QUASI-STEADY APPROXIMATION WITH REYNOLDS-DEPENDENT FRICTION FACTOR

To account for superimposed turbulent steady flow and turbulent oscillatory flow in a pipe of diameter D and cross-sectional area S in the quasi-steady approximation, the dependence

of the Moody friction factor f_M on velocity should be taken into account.

If the volume flow rate U and hence the Reynolds number N_R vary sinusoidally in time, without an additive constant, then the instantaneous friction factor $f_M(t)$ has a complicated time dependence, which has been approximated[23,33] by using a Taylor-series expansion around the peak Reynolds number $|N_{R,1}|$:

$$f_M(t) \simeq f_M + \frac{df_M}{dN_R}\,|N_{R,1}|\,(|\sin\omega t| - 1)\,, \tag{A.1}$$

where df_M/dN_R and f_M on the right side are evaluated at the peak Reynolds number. Integrating the instantaneous power dissipation over a full cycle yields the time-averaged dissipation of acoustic power per unit length arising from $\frac{1}{2}\mathrm{Re}\Big[dp_1/dx\;\widetilde{U}_1\Big]$:

$$\frac{d\dot{E}}{dx} = -\frac{2\rho_m\,|U_1|^3}{3\pi D S^2}\left[f_M - \left(1 - \frac{9\pi}{32}\right)|N_{R,1}|\,\frac{df_M}{dN_R}\right]. \tag{A.2}$$

where f_M and df_M/dN_R are evaluated at the peak Reynolds number $|N_{R,1}|$. (Note that df_M/dN_R is negative.)

It is straightforward to extend this approach to the present case of superimposed steady and oscillatory flow, for which

$$U(t) = \dot{M}/\rho_\mathrm{m} + |U_1|\sin\omega t. \tag{A.3}$$

The time-dependent friction factor is written as

$$f_M(t) \simeq f_{M,\max} + \frac{df_M}{dN_R}\,N_{R,\max}\left(\frac{\left|\dot{M}/\rho_\mathrm{m} + |U_1|\sin\omega t\right|}{\left|\dot{M}/\rho_\mathrm{m}\right| + |U_1|} - 1\right) \tag{A.4}$$

where $f_{M,\max}$ and df_M/dN_R are evaluated at the maximum Reynolds number

$$N_{R,\max} = \frac{\left(\left|\dot{M}/\rho_\mathrm{m}\right| + |U_1|\right) D\rho_\mathrm{m}}{S\mu}. \tag{A.5}$$

Then the instantaneous pressure gradient is taken to be

$$\frac{dp}{dx} = \pm f_M(t)\frac{\rho_\mathrm{m}}{2D}\frac{[U(t)]^2}{S^2}, \tag{A.6}$$

with the sign chosen so that the pressure gradient opposes the flow at that instant. The time-averaged pressure gradient is obtained by evaluating

$$\frac{dp_{2,0}}{dx} = \frac{\omega}{2\pi}\int_0^{2\pi/\omega}\frac{dp}{dx}\,dt, \tag{A.7}$$

and the dissipation of acoustic power per unit length is obtained by evaluating

$$\frac{d\dot{E}}{dx} = \frac{\omega}{2\pi}\int_0^{2\pi/\omega} \frac{dp}{dx}\,|U_1|\sin\omega t\; dt. \tag{A.8}$$

The integrations are performed piecewise between the zero crossings of $U(t)$ if they exist, as in Eqs. (8) and (17). With $\varepsilon = \dot{M}/\rho_{\rm m}\,|U_1|$, the results are

$$\frac{dp_{2,0}}{dx} = -\,\mathrm{sign}(\varepsilon)\frac{\dot{M}^2}{2\rho_{\rm m}DS^2}\left[\left(1+\frac{1}{2\varepsilon^2}\right)f_{M,\max} - \frac{2\varepsilon^2-2\,|\varepsilon|+1}{2\varepsilon^2(1+|\varepsilon|)}\frac{df_M}{dN_R}\,N_{R,\max}\right],\quad |\varepsilon|\ge 1; \tag{A.9}$$

$$= -\,\mathrm{sign}(\varepsilon)\frac{\dot{M}^2}{2\rho_{\rm m}DS^2}\left[\frac{(1+2\varepsilon^2)\sin^{-1}|\varepsilon| + 3\,|\varepsilon|\sqrt{1-\varepsilon^2}}{\pi\varepsilon^2}f_{M,\max}\right.$$
$$\left. + \frac{\pi\,|\varepsilon|\,(3/2+\varepsilon^2) - 3\,|\varepsilon|\,(1+|\varepsilon|)\sqrt{1-\varepsilon^2} - (1+|\varepsilon|)\,(1+2\varepsilon^2)\sin^{-1}|\varepsilon|}{\pi\varepsilon^2(1+|\varepsilon|)}\frac{df_M}{dN_R}\,N_{R,\max}\right],$$
$$|\varepsilon|\le 1, \tag{A.10}$$

and

$$\frac{d\dot{E}}{dx} = -\frac{\rho_{\rm m}\,|U_1|^3}{2DS^2}\left[|\varepsilon|\,f_{M,\max} + \frac{(3-2\,|\varepsilon|)\,(1-2\,|\varepsilon|)}{8(1+|\varepsilon|)}\frac{df_M}{dN_R}\,N_{R,\max}\right],\quad |\varepsilon|\ge 1, \tag{A.11}$$

$$= -\frac{2\rho_{\rm m}\,|U_1|^3}{3\pi DS^2}\left\{\left[\left(1+\frac{\varepsilon^2}{2}\right)\sqrt{1-\varepsilon^2} + \frac{3}{2}\varepsilon\sin^{-1}\varepsilon\right]f_{M,\max}\right.$$
$$\left. - \left[\left(1+\frac{\varepsilon^2}{2}\right)\sqrt{1-\varepsilon^2} + \frac{3}{2}\varepsilon\sin^{-1}\varepsilon - \frac{9\pi}{32}\frac{1+4\varepsilon^2}{1+|\varepsilon|}\right]\frac{df_M}{dN_R}\,N_{R,\max}\right\},\quad |\varepsilon|\le 1. \tag{A.12}$$

Equations (A.9)–(A.12) reduce to Eqs. (13), (14) and (18)–(20) for $df_M/dN_R = 0$ if $f_M\,dx/D$ is associated with K. Equation (A.12) reduces to Eq. (A.2) if $\varepsilon = 0$.

Viscous power dissipation can be written as $d\dot{E}/dx = -r_\nu\,|U_1|^2/2$, where r_ν is the resistance per unit length, suggesting that Eqs. (A.11)–(A.12) should be expressed as

$$r_{\nu,\rm turb} = \frac{\rho_{\rm m}\,|U_1|}{DS^2}\left[|\varepsilon|\,f_{M,\max} + \frac{(3-2\,|\varepsilon|)\,(1-2\,|\varepsilon|)}{8(1+|\varepsilon|)}\frac{df_M}{dN_R}\,N_{R,\max}\right],\quad |\varepsilon|\ge 1, \tag{A.13}$$

$$= \frac{4\rho_{\rm m}\,|U_1|}{3\pi DS^2}\left\{\left[\left(1+\frac{\varepsilon^2}{2}\right)\sqrt{1-\varepsilon^2} + \frac{3}{2}\varepsilon\sin^{-1}\varepsilon\right]f_{M,\max}\right.$$
$$\left. - \left[\left(1+\frac{\varepsilon^2}{2}\right)\sqrt{1-\varepsilon^2} + \frac{3}{2}\varepsilon\sin^{-1}\varepsilon - \frac{9\pi}{32}\frac{1+4\varepsilon^2}{1+|\varepsilon|}\right]\frac{df_M}{dN_R}\,N_{R,\max}\right\},\quad |\varepsilon|\le 1. \tag{A.14}$$

When this is compared to the equivalent result for laminar flow in the boundary-layer approximation,[33] it is apparent that this model of turbulence multiplies the power dissi-

pation $d\dot{E}/dx$ and the resistance per unit length by a factor

$$m = \frac{\delta_\nu N_{R,\max}}{4D}\left[|\varepsilon|\, f_{M,\max} + \frac{(3-2\,|\varepsilon|)\,(1-2\,|\varepsilon|)}{8(1+|\varepsilon|)}\frac{df_M}{dN_R}\,N_{R,\max}\right],\ \ |\varepsilon| \geq 1, \tag{A.15}$$

$$= \frac{\delta_\nu N_{R,\max}}{3\pi D}\left\{\left[\left(1+\frac{\varepsilon^2}{2}\right)\sqrt{1-\varepsilon^2} + \frac{3}{2}\varepsilon\sin^{-1}\varepsilon\right] f_{M,\max}\right.$$

$$\left. - \left[\left(1+\frac{\varepsilon^2}{2}\right)\sqrt{1-\varepsilon^2} + \frac{3}{2}\varepsilon\sin^{-1}\varepsilon - \frac{9\pi}{32}\frac{1+4\varepsilon^2}{1+|\varepsilon|}\right]\frac{df_M}{dN_R}\,N_{R,\max}\right\},\ \ |\varepsilon| \leq 1. \tag{A.16}$$

At low enough velocities, $m \to 1$; at lower velocities the flow is laminar. The $m = 1$ boundary between the laminar and turbulent zones occurs roughly at

$$|N_{R,\max}| \simeq 2000 \text{ for } D/\delta_\nu < 4, \tag{A.17}$$

$$\frac{|N_{R,\max}|}{D/\delta_\nu} \simeq 500 \text{ for } D/\delta_\nu > 4. \tag{A.18}$$

---

* Electronic address: swift@lanl.gov; URL: www.lanl.gov/thermoacoustics/

[1] G. Walker. *Stirling Engines.* Clarendon, Oxford, 1960.

[2] J. R. Senft. *Ringbom Stirling Engines.* Oxford University Press, 1993.

[3] G. Walker. *Cryocoolers.* Plenum, New York, 1983.

[4] Ivo Kolin. *The Evolution of the Heat Engine.* Longman, London, 1972.

[5] R. Radebaugh. A review of pulse tube refrigeration. *Adv. Cryogenic Eng.*, 35:1191–1205, 1990.

[6] G. W. Swift. Thermoacoustic engines. *J. Acoust. Soc. Am.*, 84:1145–1180, 1988.

[7] I. Urieli and D. M. Berchowitz. *Stirling Cycle Engine Analysis.* Adam Hilger, Bristol UK, 1984.

[8] C. M. de Blok. Thermoacoustic system, 1998. Dutch Patent: International Application Number PCT/NL98/00515. US Patent 6,314,740, November 13, 2001.

[9] T. Yazaki, A. Iwata, T. Maekawa, and A. Tominaga. Traveling wave thermoacoustic engine in a looped tube. *Phys. Rev. Lett.*, 81:3128–3131, 1998.

[10] S. Backhaus and G. W. Swift. A thermoacoustic-Stirling heat engine: Detailed study. *J. Acoust. Soc. Am.*, 107:3148–3166, 2000.

[11] G. W. Swift, D. L. Gardner, and S. Backhaus. Acoustic recovery of lost power in pulse tube refrigerators. *J. Acoust. Soc. Am.*, 105:711–724, 1999.

[12] J. Wurm, J. Kinast, T. Roose, and W. Staats. *Stirling and Vuilleumier Heat Pumps.* McGraw-Hill, New York, 1991.

[13] K. M. Godshalk, C. Jin, Y. K. Kwong, E. L. Hershberg, G. W. Swift, and R. Radebaugh. Characterization of 350 Hz thermoacoustic driven orifice pulse tube refrigerator with measurements of the phase of the mass flow and pressure. *Adv. Cryogenic Eng.*, 41:1411–1418, 1996.

[14] F. P. Incropera and D. P. DeWitt. *Introduction to Heat Transfer.* Wiley, 2nd edition, 1990.

[15] M. P. Mitchell. Pulse tube refrigerator, 1999. US Patent No. 5,966,942; continuation in part 6,109,041.

[16] N. Tesla. Valvular conduit, February 1920. US Patent number 1,329,559.

[17] A. Petculescu and L. A. Wilen. Oscillatory flow in jet pumps: Nonlinear effects and minor losses. *J. Acoust. Soc. Am.*, 113:1282–1292, 2003.

[18] What acousticians call the volume velocity is known as the volume flow rate in fluid mechanics. Its dimensions are volume per unit time.

[19] Size 16 (one inch) VCO Couplings, Swagelok Company, Solon OH, www.swagelok.com.

[20] Endevco, San Juan Capistrano, CA.

[21] Model SR830, Stanford Research Systems, Sunnyvale CA, www.srsys.com.

[22] Consistent with Ref. 33, this article uses notation such as $p(t) = p_{\rm m}+{\rm Re}[p_1 e^{i\omega t}] + p_{2,0}+{\rm Re}[p_{2,2} e^{i2\omega t}] + ...$ for time-dependent variables. The subscript "m" indicates a mean value that exists independent of the wave. The subscript "2,0" indicates a second-order, time-averaged correction to the mean value, caused by the wave.

[23] W. C. Ward and G. W. Swift. Design environment for low amplitude thermoacoustic engines (DeltaE). *J. Acoust. Soc. Am.*, 95:3671–3672, 1994. Software and user's guide available either from the Los Alamos thermoacoustics web site at www.lanl.gov/thermoacoustics/ or from the Energy Science and Technology Software Center, US Department of Energy, Oak Ridge, Tennessee.

[24] T. G. Wang and C. P. Lee. Radiation pressure and acoustic levitation. In M. F. Hamilton and D. T. Blackstock, editors, *Nonlinear Acoustics*, pages 177–205. Academic Press, 1998.

[25] L. D. Landau and E. M. Lifshitz. *Fluid Mechanics.* Pergamon, 1982. Sec. 64.

[26] R. W. Fox and A. T. McDonald. *Introduction to Fluid Mechanics.* Wiley, 1985.

[27] Model SRFG-348/5 rectangular silicone rubbber heaters, Omega Engineering, Stamford Connecticut. www.omega.com.

[28] Ohio Semitronics, Hilliard OH.

[29] Model C2, Clever Fellows Innovation Consortium, Inc., Troy NY, www.cficinc.com.

[30] Schaevitz Model 500 HR, Measurement Specialties, Inc., Fairfield NJ, www.schaevitz.com.

[31] A. M. Fusco, W. C. Ward, and G. W. Swift. Two-sensor power measurements in lossy ducts. *J. Acoust. Soc. Am.*, 91:2229–2235, 1992.

[32] I. E. Idelchik. *Handbook of Hydraulic Resistance*. Begell House, New York, 3rd edition, 1994.

[33] G. W. Swift. *Thermoacoustics: A Unifying Perspective for some Engines and Refrigerators*. Acoustical Society of America Publications, Sewickley PA, 2002.

[34] V. L. Streeter. *Handbook of Fluid Dynamics*. McGraw-Hill, 1961.

[35] B. L. Smith and A. Glezer. The formation and evolution of synthetic jets. *Phys. Fluids*, 10:2281–2297, 1998.

[36] B. L. Smith and G. W. Swift. Power dissipation and time-averaged pressure in oscillating flow through a sudden area change. *J. Acoust. Soc. Am.*, 113:2455–2463, 2003.

[37] Indeed, we *did* originally expect this, until experimental results induced us to consider the question more carefully.

[38] Equation 19, with the choices for K_+ and K_- described below Eq. (11), account for minor-loss effects at the small ends of the gas diodes, but not for the surface-induced friction factor in the conical portions.

[39] In U.S. Patent No. 6,637,211, "Circulating heat exchangers for oscillating wave engines and refrigerators" by G. W. Swift and S. N. Backhaus, Eqs. (4) and (5) are incorrect. Equations (16) and (17) here give the correct definition of acoustic power for a volume velocity equal to the sum of a time-independent term and a sinusoidal term.

[40] R. T. Muehleisen and A. A. Atchley. Fundamental azimuthal modes of a constricted annular resonator: Theory and measurement. *J. Acoust. Soc. Am.*, 109:480–487, 2001.

[41] P. M. Morse and K. U. Ingard. *Theoretical Acoustics*. McGraw-Hill, 1968.

[42] B. L. Smith and G. W. Swift. Measuring second-order time-average pressure. *J. Acoust. Soc. Am.*, 110:717–723, 2001.

[43] T. J. Hofler. *Thermoacoustic refrigerator design and performance*. PhD thesis, Physics department, University of California, San Diego, 1986.

[44] J. R. Olson and G. W. Swift. Similitude in thermoacoustics. *J. Acoust. Soc. Am.*, 95:1405–1412, 1994.

[45] The thermoacoustic-Stirling engine described by S. Backhaus and G. W. Swift in "A thermoacoustic-Stirling heat engine: Detailed study," J. Acoust. Soc. Am. Vol. 107, 3148-3166 (2000), is now operating with a half-wavelength, one-diode hot heat transfer loop in place of its original internal electric-resistance hot heat exchanger. The performance of this hardware is described in "A self-circulating heat exchanger for use in Stirling and thermoacoustic-Stirling engines," S. Backhaus and R. S. Reid, in preparation for Space Technology International Forum 2005.

Table I. Contributions to $p_{2,0}$ in Fig. 6.

	each	× mult =	net
Reversible:			
Pipe, Eq. (1)	±5.0 kPa	×2 =	0.00 kPa
Cones, Eq. (1)	±10.0 kPa	×2 =	0.00 kPa
Irreversible:			
Gas diodes	+1.68 kPa	×2 =	+3.36 kPa
Pipe			−2.30 kPa
Cones	−0.28 kPa	×2 =	−0.56 kPa
Elbows	−0.085 kPa	×4 =	−0.34 kPa
Exit to mix. ch.			−0.16 kPa
Total:			0.00 kPa

FIGURE CAPTIONS

Figure 1. (a) A portion of an oscillating-gas engine or refrigerator, containing a shell-and-tube heat exchanger or other traditional cross-flow heat exchanger. The heat exchanger is below a stack or regenerator, and is above a pulse tube, thermal buffer tube, or open duct. The oscillating flow of the working gas (e.g., pressurized helium) is vertical throughout. The steady flow of the process fluid (e.g., water) is horizontal through the heat exchanger. (b) A portion of an oscillating-gas engine or refrigerator, in which the traditional heat exchanger has been replaced by a single external pipe one wavelength long. Gas diodes at the velocity maxima create mean flow, which steadily transfers heat between the process fluid outside the pipe and the engine or refrigerator to which the pipe ends are attached. (c) Qualitative plot of volume velocity U as a function of location x in the pipe, at four equally spaced times t during a cycle of the wave. The zero of time phase is when the pressure in the mixing chamber is a maximum.

Figure 2. Scale drawings of the apparatus. (a) Overview of the entire apparatus, except for the linear motor and its pressure housing below the bottom. The gas diodes were located 1/4 and 3/4 of the way around the loop of piping, and the valve was halfway around. The locations of most of the thermocouples ("T") and pressure sensors ("P") in the apparatus are shown in this view. The four long, straight runs of pipe (each having five thermocouples) were wrapped with heating blankets. The entire loop was then wrapped with thermal insulation. However, for some measurements, four alternative straight runs of pipe were used, each having a water jacket instead of the thermocouples, heater blanket, and insulation. The spatial extent of the heating blankets and water jackets are shown in the upper right. (b) Detailed view of one of the gas diodes, also showing how the fittings come apart. (c) Detailed view of the drive assembly. The piston, driven by a linear motor, insonified the apparatus. The two optional heat exchangers rejected heat to flowing water at ambient temperature. Temperature and pressure sensors not shown in (a) are shown here. Bolts holding the drive assembly together are not shown.

Figure 3. A typical wave, with 2.4-MPa argon at 48.4 Hz, using the water-cooled loop and with the valve closed to enforce zero mean flow, as a function of position around the loop, with $x = 0$ and $x = 6.33$ m where the loop meets the mixing chamber. Both gas diodes

were oriented to encourage flow in the positive-x direction, with their small ends toward smaller x. (a) Real and imaginary parts of the pressure wave. Points are measured values and lines are calculations. (b) Calculated real and imaginary parts of the volume-velocity wave. In (a) and (b), the standing-wave components are so much larger than the out-of-phase components that the latter have been multiplied by 10 for clarity. The zero of time phase is chosen so that the pressure oscillations in the mixing chamber are real. (c) The time-averaged pressure as a function of position, relative to its value in the mixing chamber. Points are measured values and lines are calculations. The two vertical dotted lines are at the small-x, small-diameter ends of the gas diodes. The vertical discontinuity is at the valve.

Figure 4. Temperature T as a function of position x around the loop for three baseline circumstances with the valve closed. Open circles: no acoustic power, 41 W applied with electric heaters, 1.15 W/°C insulation. Inverted triangles: No electric heat, 53 W of acoustic power applied with piston ($|p_1| = 152$ kPa in the mixing chamber), 2 W/°C insulation. Erect triangles: No electric heat, 124 W of acoustic power applied with piston ($|p_1| = 207$ kPa in the mixing chamber), 2 W/°C insulation. The points at $x = 0$ and $x = 6.33$ m are temperatures inside the mixing chamber; other points are temperatures on the wall of the loop.

Figure 5. Acoustic power delivered by the piston, $\dot{E}_{\rm pist}$, as a function of acoustic power delivered to the dummy load, $\dot{E}_{\rm load}$. Circles, $|p_1| = 170$ kPa in the mixing chamber. Squares, $|p_1| = 240$ kPa in the mixing chamber. The straight line, a guide to the eye, has a slope of unity and an arbitrary vertical offset.

Figure 6. (a)–(c) A typical wave, with 2.4-MPa argon at 48.1 Hz, using the water-cooled pipes and with the valve open to allow $\dot{M} \neq 0$. The two gas diodes were oriented to encourage flow in the positive-x direction, with their small ends toward smaller x. (a) Real and imaginary parts of the pressure wave as a function of position around the loop. Points are measured values and lines are calculations. (b) Calculated real, imaginary, and mean parts of the volume velocity. In (a) and (b), the standing-wave components are so much larger than the out-of-phase components that the latter have been multiplied by 3 for clarity. The zero of phase is chosen so that the pressure oscillations in the mixing chamber are real. (c) The time-averaged pressure as a function of position, relative to its value in the mixing chamber. Points are measured values and lines are calculations. The two vertical

dotted lines are at the small-x, small-diameter ends of the gas diodes. (d) Temperature as a function of position around the loop, with the insulated pipes and the 2 W/°C insulation, under conditions similar to that of (a)–(c). Filled symbols are temperatures measured on the metal surface of the loop and open symbols are temperatures measured in the gas. Gas temperatures at $x = 0$ and $x = 6.33$ m are those at 5 locations in the mixing chamber. Circles, no electric heat. Squares, 79 W electric heat. Erect triangles, 167 W electric heat. Inverted triangles, 252 W electric heat. The curves represent calculated estimates corresponding to the erect triangles, as explained in the text.

Figure 7. The part of $\mathrm{Im}[p_1]$ near the gas diodes that is associated with $\dot{M} \neq 0$, as a function of the amplitude of the wave. The horizontal axis is the amplitude of the pressure oscillation in the mixing chamber, raised to the 3/2 power. The four sets of symbols (measurements) and the four curves (calculations) correspond to the four pressure transducers closest to the two gas diodes. The measurements were taken with the water-cooled pipes.

Figure 8. Time-averaged pressure difference across the gas diodes as a function of the normalized square of the amplitude of the oscillating pressure in the mixing chamber. Filled symbols, valve closed. Open symbols, valve open. Erect triangles, gas diode near $x = 1.6$ m. Inverted triangles, gas diode near $x = 4.8$ m. Lines, corresponding calculations using Eq. (10) (plus, for the lower line, the small calculated steady-flow pressure difference across the cone and pipe segments between the pressure transducers).

Figure 9. Mass flow around the loop as a function of pressure amplitude in the mixing chamber. Symbols are based on measured electric heat and temperature rise, with the insulated pipes and the 1.15 W/°C insulation. Lines represent calculations, based on two different sets of assumptions described in the text.

Figure 10. Acoustic power as a function of the cube of the pressure amplitude in the mixing chamber. Symbols are measured acoustic power delivered by the piston. Experimental uncertainties are about 2%. Erect triangles, valve open; inverted triangles, valve closed. Lines are calculated acoustic power dissipation due to several sources. Short dashed lines, valve closed; long dashed lines, valve open.

Figure 11. The calculated energy efficiency of the gas-diode pump as a function of $\varepsilon = \dot{M}/\rho_\mathrm{m}\,|U_1|$ and $\beta = (K_- - K_+)/(K_- + K_+)$.

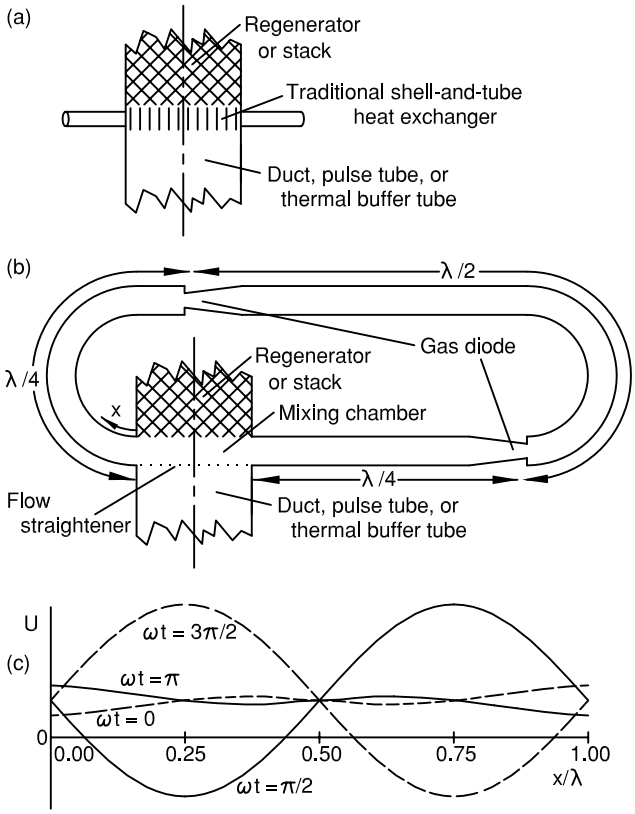

Figure 1
Swift and Backhaus
J. Acoust. Soc. Am.

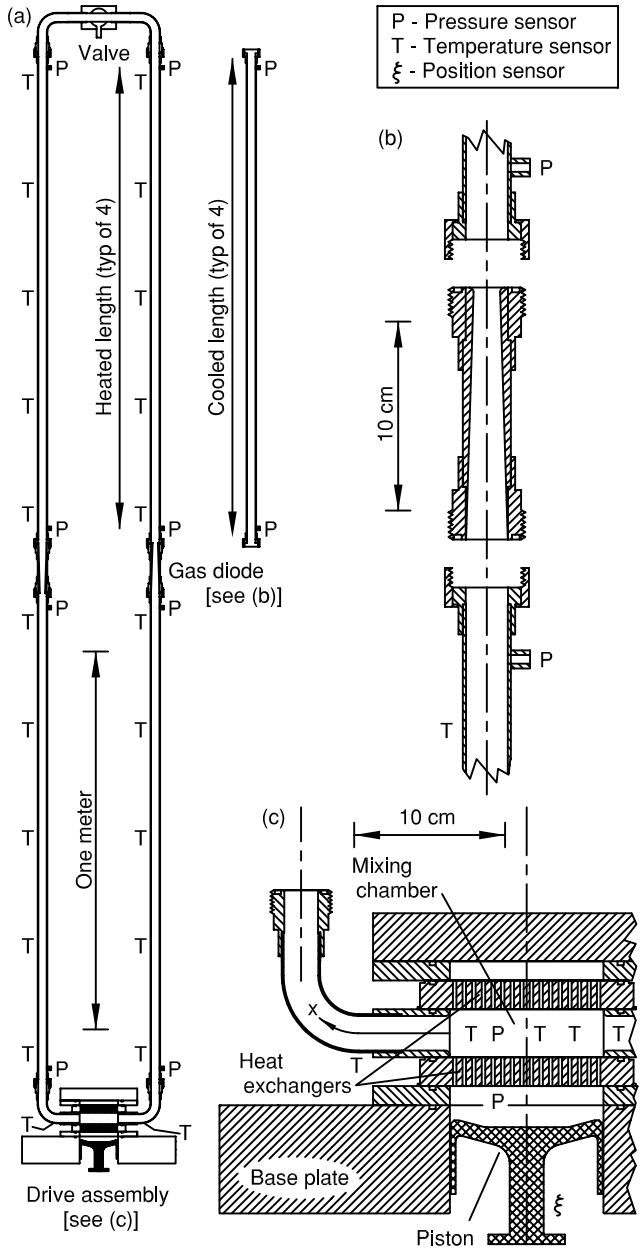

Figure 2
Swift and Backhaus
J. Acoust. Soc. Am.

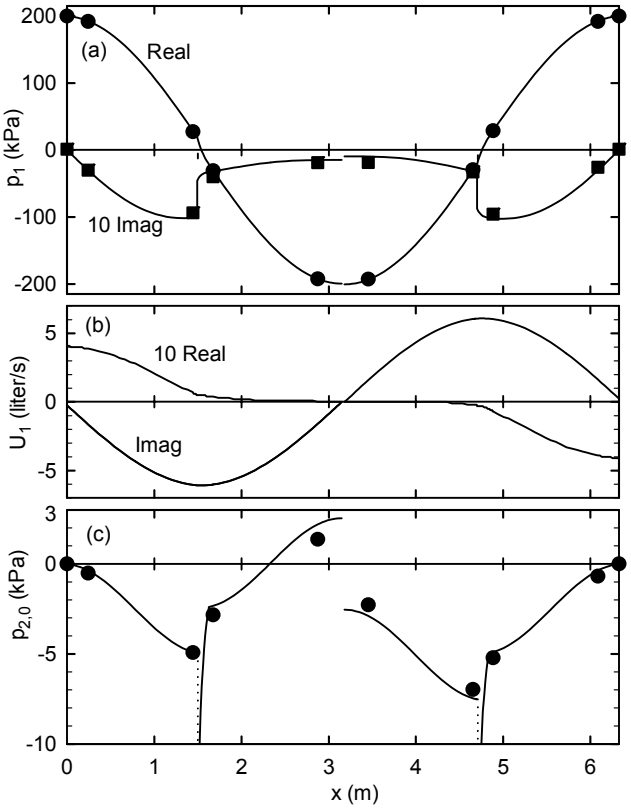

Figure 3
Swift and Backhaus
J. Acoust. Soc. Am.

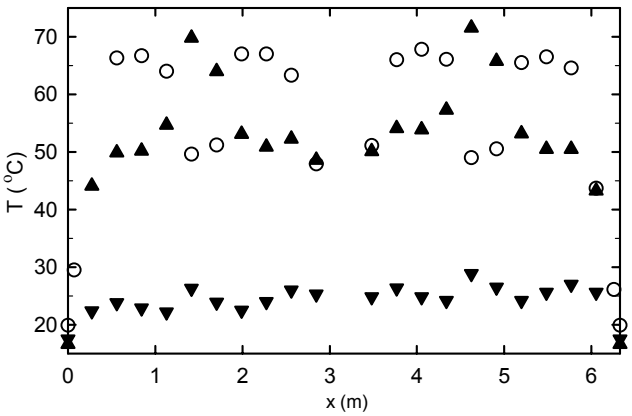

Figure 4
Swift and Backhaus
J. Acoust. Soc. Am.

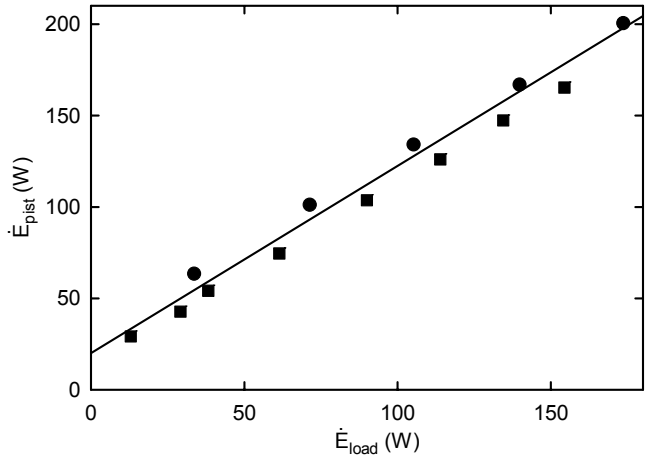

Figure 5
Swift and Backhaus
J. Acoust. Soc. Am.

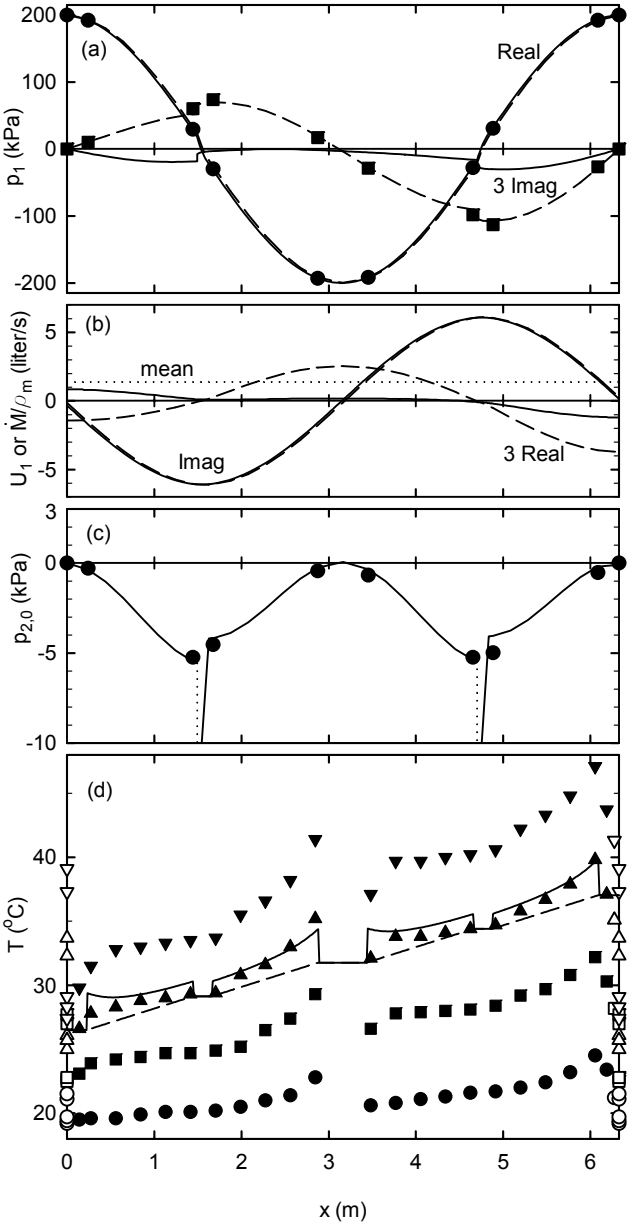

Figure 6
Swift and Backhaus
J. Acoust. Soc. Am.

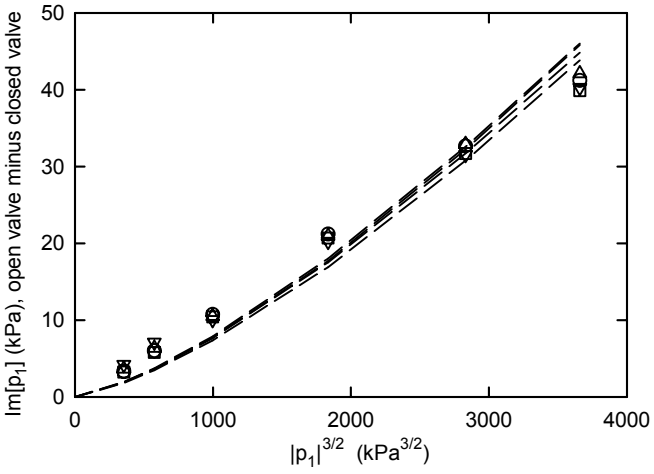

Figure 7
Swift and Backhaus
J. Acoust. Soc. Am.

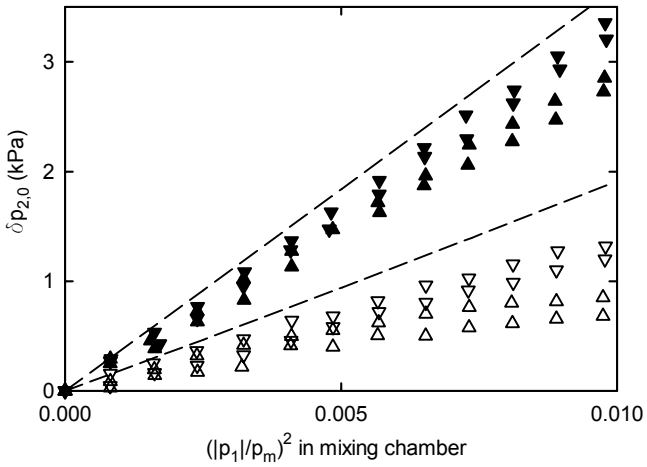

Figure 8
Swift and Backhaus
J. Acoust. Soc. Am.

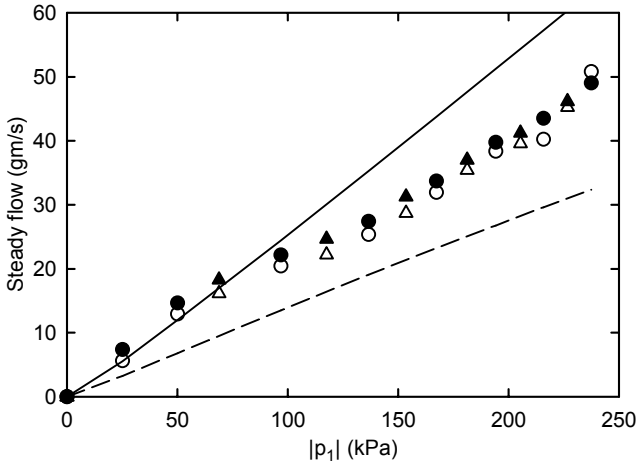

Figure 9
Swift and Backhaus
J. Acoust. Soc. Am.

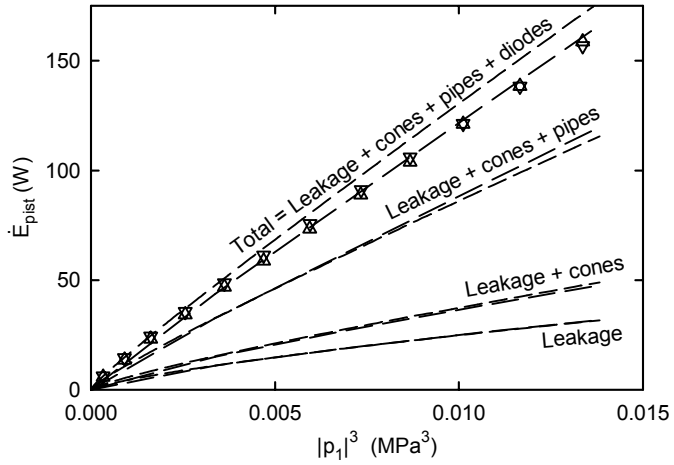

Figure 10
Swift and Backhaus
J. Acoust. Soc. Am.

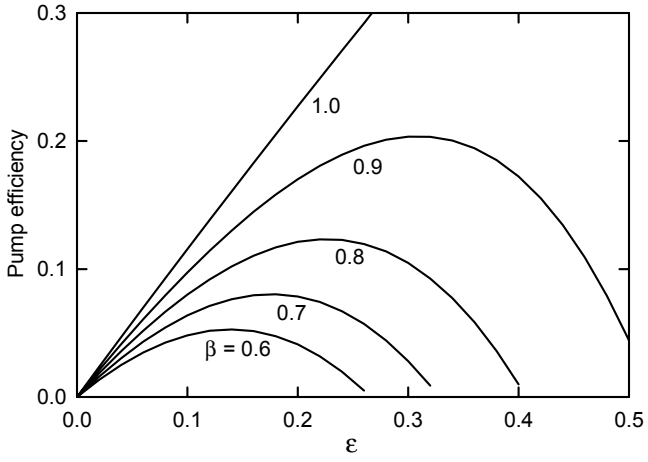

Figure 11
Swift and Backhaus
J. Acoust. Soc. Am.